Monami as an oscillatory hydrodynamic instability in a submerged sea grass bed

Shreyas Mandre

Brown University, Providence RI 02912 USA

The onset of *monami* – the synchronous waving of sea grass beds driven by a steady flow – is modeled as a linear instability of the flow. Our model treats the drag exerted by the grass in establishing the steady flow profile, and in damping out perturbations to it. This damping leads to a finite threshold flow for the instability, which agrees with experimental observations. This role of vegetation drag differentiates our mechanism from the previous hypothesis that the Kelvin-Helmholtz instability underlies *monami*.

(80) Sea grasses exhibit a rich set of dynamical behavior due to their collective interaction with fluid flows. The hydrodynamic processes resulting from this behavior influence many environmental processes such as sedimentation, transportation of dissolved oxygen, plant growth, and biomass production Fonseca & Kenworthy (1987); Grizzle *et al.* (1996); Nepf (1999, 2012). One such response of the submerged grass beds to steady currents is the formation of coherent large amplitude oscillations, known as *monami* Ackerman & Okubo (1993). In this letter, we provide a hydrodynamic mechanism for the onset of these coherent oscillations.

(77) Current explanations of *monami* invoke the existence of a free shear layer at the top of the grass bed (henceforth called grass top) due to vegetation drag Ikeda & Kanazawa (1996); M. Ghisalberti and H. M. Nepf (2002); Raupach *et al.* (1996). Its instability, through a mechanism similar to the Kelvin-Helmholtz instability, is thought to lead to coherent eddies over the grass bed, and drive large amplitude synchronous oscillations. This model has been applied to predict the observed frequency of *monami* and to understand transport in the seagrass bed Nepf & Vivoni (2000); M. Ghisalberti and H. M. Nepf (2002); Ghisalberti & Nepf (2004); Okamoto *et al.* (2012).

(126) However, several aspects of this explanation remain unsatisfactory: (i) The velocity profile of the free shear layer is assumed *ad hoc* to be piecewise linear Py *et al.* (2006) or hyperbolic tangent M. Ghisalberti and H. M. Nepf (2002); Raupach *et al.* (1996). (ii) The role of drag in damping the coherent perturbations to the shear profile is sometimes ignored Raupach *et al.* (1996). (iii) No existing theory explains the threshold flow speed, observed in the lab M. Ghisalberti and H. M. Nepf (2002) and the field Grizzle *et al.* (1996), below which *monami* is not observed. (iv) The thickness of the free shear layer is in many cases comparable to the unvegetated water depth, and therefore inconsistent with the definition of the free shear layer. Here we present a mathematical model for the linear instability that accounts correctly for these effects, while also explaining lab experiments and field observations.

(86) Although *monami* is manifest in the motion of the grass, the drag exerted by the grass bed on the flow is central to the hypothesized instability. The instability and the resulting flow structures persist in lab experiments even when flexible grass mimics are replaced by rigid dowels M. Ghisalberti and H. M. Nepf (2002); Ghisalberti & Nepf (2006). Therefore, to develop the essential mathematical model, we assume the grass
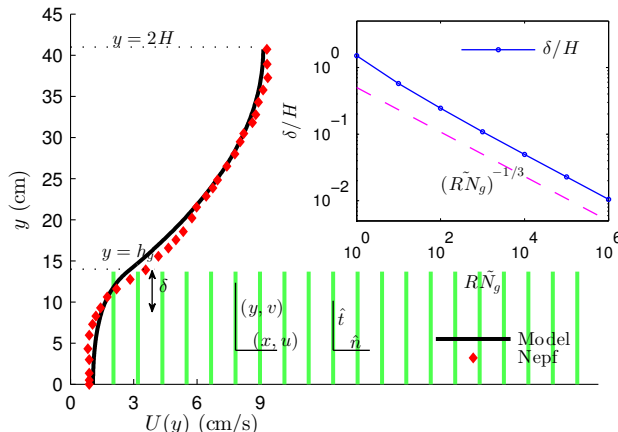
FIGURE 1. **(111)** Schematic setup and comparison of our steady flow profile with that from the experiments in ref. Ghisalberti & Nepf (2004) (Case I from Table 1) and its approximation with $U_0 = 7.28$ cm/s and $\delta = 5.02$ cm in our model. The grass extends up to $y = h_g$ in the water column of depth $2H$. The steady velocity profile can be decomposed into a parabolic profile in the unvegetated region, a uniform profile deep within the vegetation, and a boundary layer of thickness δ near the grass top. The dependence of the boundary layer thickness (estimated as $|U/U_y|$ at $y = h_g$ from the numerical solution of (0.2)) on the vegetation density parameter $Re\tilde{N}_g$ is shown in the inset.
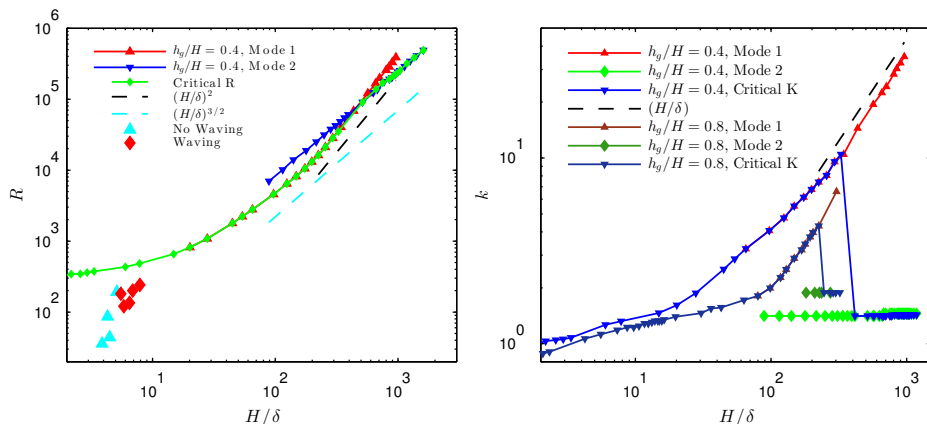

FIGURE 2. **(105)** Critical Reynolds number (top) and the corresponding marginally stable wave number (bottom) for different submergence ratio as a function of vegetation density parametrized by the boundary layer thickness. Parameters from experiments reported in ref. M. Ghisalberti and H. M. Nepf (2002) to exhibit or suppress synchronous waving are also included in the top panel. Inset compares experimental observations of the experimentally measured dominant frequency f_o (in Hz) with the predictions $f_p = \text{Im}(\sigma)$ from the solution of (0.3). The experimental data in the inset is obtained from refs. M. Ghisalberti and H. M. Nepf (2002) (Ghisalberti) and Vivoni (1998) (Vivoni). In order to estimate the Re for these experiments, a representative value of $\mu = 0.1$ Pa s was assumed.

blades to be rigid, on average oriented vertically. We show that the drag of the grass results in an instability mode different from the Kelvin-Helmholtz instability.

(27) The drag exerted by the vegetation, assumed dense, is modeled by a continuous
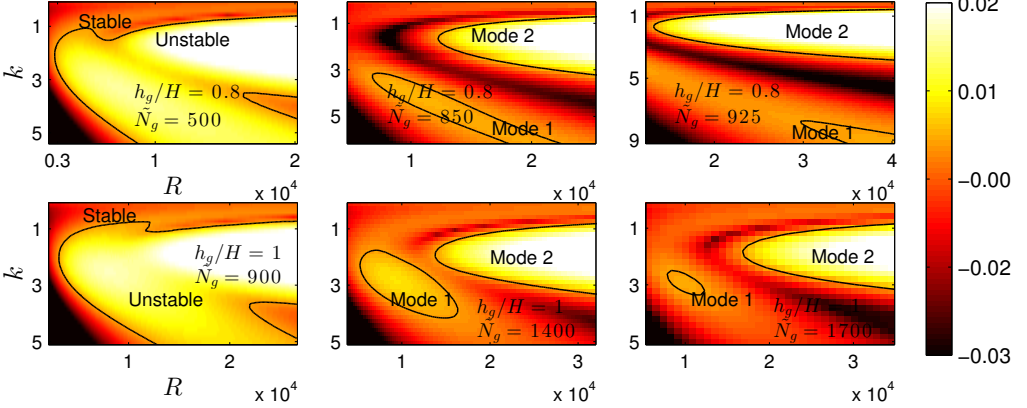
FIGURE 3. **(46)** $Re(\sigma)$ and the neutral curve ($Re(\sigma)=0$) as function of wavenumber and Re for parameters shown in the corresponding panel. As $\tilde{N}_g$ increases, the unstable region splits into two labeled as "Mode 1" and "Mode 2". For $\tilde{N}_g$ below (above) a critical value, Mode 1 (Mode 2) sets the threshold Re.

body force **f**. This drag enters the fluid mass and momentum balance equations as

$$\nabla \cdot \mathbf{u} = 0, \quad \rho\left(\mathbf{u}_t + \mathbf{u}.\nabla\mathbf{u}\right) = -\nabla p + \mu\nabla^2\mathbf{u} + \mathbf{f} + \rho\mathbf{g} \tag{0.1}$$

(138) where ρ, $\mathbf{u}$, and p are the fluid density, velocity, and pressure respectively, μ the dynamic eddy viscosity and $\mathbf{g}$ the acceleration due to gravity. The Reynolds number of the flow based on the scale of the grass blade is $O(10^2 - 10^3)$; therefore, neglecting the skin friction, we model it as the form drag on the vegetation, $\mathbf{f} = N_g C_N \rho u |u| d\hat{\boldsymbol{x}}$ Nepf (1999); Nepf & Vivoni (2000); Ghisalberti & Nepf (2004), where N_g is the blade number density per unit horizontal area, C_N the drag coefficient, and d the average blade width projected perpendicular to the flow. In the interest of simplicity, we model the turbulence using an eddy viscosity. In the field, both C_N, N_g and μ vary with position, but we do not expect these variations to be central to the instability mechanism, and therefore take them to be constants. Based on previous experiments Vivoni (1998); Nepf & Vivoni (2000), we take $C_N = 1$.

   (19) We first calculate the fully developed steady solution $\mathbf{u} = U(y)\hat{\boldsymbol{x}}$ of (0.1) driven by constant pressure gradient dP/dx, satisfying

$$-\frac{dP}{dx} + \mu U''(y) + S(y)\rho C_N dN_g U|U| = 0 \tag{0.2}$$

(318) where $S(y) = 1$ for $0 < y < h_g$ and $S(y) = 0$ for $h_g < y < 2H$. Eq. (0.2) is solved subject to no shear at the boundaries, i.e., $U'(0) = U'(2H) = 0$. The former arises for dense vegetation because the shear stress exerted by the bottom surface is expected to be negligible compared to the vegetation drag Nepf & Vivoni (2000), whereas the latter models the free interface. A comparison of the steady flow profile from the solution of (0.2) with experimental measurements is shown in Fig. 1. The profile $U(y)$ has three distinct regions. Within vegetation, it is approximately uniform with $U(y) \approx U_g = \sqrt{\frac{dP/dx}{\rho C_N dN_g}}$, arising from balancing the drag with pressure gradient. Outside the vegetation, the velocity has a simple parabolic profile. At the grass top, continuity of shear stresses results in a boundary layer of thickness δ. Denoting U_{bl} to be the velocity scale in the boundary layer, and $U_0 = (dP/dx) H^2/\mu$ the velocity scale in the unvegetated region, the balance between viscous forces and vegetation drag implies ($\mu U_{\mathrm{bl}}/\delta^2 \sim \rho C_N dN_g U_{\mathrm{bl}}^2$),

and the continuity of shear stress across the grass top implies ($U_{\text{bl}}/\delta \sim U_0/H$). Solving for δ and U_{bl} yields $\delta/H = U_{\text{bl}}/U_0 = (Re\tilde{N}_g)^{-1/3}$, where $\tilde{N}_g = (C_N d H N_g)$ is the vegetation frontal area per bed area, and $Re = \rho U_0 H/\mu$ is the Reynolds number of the flow. A numerical estimate of δ (U/U_y at $y = h_g$) is compared with this prediction in Fig. 1 (inset). Because this boundary layer develops independent of the influence of the boundaries, we identify it to be analogous to the free shear layer M. Ghisalberti and H. M. Nepf (2002); Ghisalberti & Nepf (2004) in the previous explanation of *monami*. This dependence of δ on N_g, verified in Fig. 1, gives us a way to systematically investigate the effect of the shear layer thickness on the instability mechanism. The figure also shows that the asymptotic regime of a thin boundary layer is expected to hold for $Re\tilde{N}_g \gtrsim 100$. In this notation, $U_g/U_0 = (Re\tilde{N}_g)^{-1/2}$ (used for deriving (0.5)).

(27) Next we substitute $\mathbf{u} = (U + \tilde{u}, \tilde{v})$, $p = P + \tilde{p}$ in (0.1) and expand to linear order to investigate the evolution of small perturbations $(\tilde{u}, \tilde{v})$, which obey

$$\rho(u_t + U u_x + v U_y) = -p_x + \mu\nabla^2 u - 2S\rho C_N d N_g U u,$$
$$\rho(v_t + U v_x) = -p_y + \mu\nabla^2 v, \quad \nabla \cdot \mathbf{u} = 0,$$

(89) where the tilde are dropped. These equations are non-dimensionalized using half channel height H, velocity U_0, and time H/U_0, leading to three non-dimensional parameters, *viz.* Re, $\tilde{N}_g$, and the vegetation submergence ratio h_g/H. We also use δ/H in lieu of $\tilde{N}_g$ to parametrize the vegetation density and help elucidate the instability mechanism. Using a stream function ψ with $u = \psi_y, v = -\psi_x$ to satisfy mass balance, we seek a solution of the form $(u, v, \psi) = (\hat{u}(y), \hat{v}(y), \phi(y))\, e^{ikx+\sigma t}$ to obtain a modified Orr-Sommerfield equation Drazin & Reid (1981)

$$\left(D^2 - k^2\right)^2 \phi = Re\left[(\sigma + ikU)\left(D^2 - k^2\right) - ikU_{yy}\right]\phi \\ + D\left(2R\tilde{N}_g S U D\phi\right), \tag{0.3}$$

(47) where $D = d/dy$, and subject to the boundary conditions $D\phi = D^2\phi = 0$ at $y = 0$ and $y = 2$. The growth rate σ for a given wave number k appears as an eigenvalue that allows a non-trivial solution ϕ of (0.3). We solve (0.3) numerically for σ and ϕ.

(155) A threshold in Re, above which the flow is unstable ($\text{Re}(\sigma) > 0$) for at least one k, emerges from the solution of (0.3). The dependence of this threshold Re, and the corresponding marginally stable wavenumber k, on δ/H and h_g/H is shown in Fig. 2, and is found to compare well with experimental observations M. Ghisalberti and H. M. Nepf (2002). The threshold Re increases with the vegetation density, indicating a competition between the destabilizing shear in the flow, and the stabilizing effect of damping due to vegetation drag. A similar conclusion was presented for an analogous problem (flow around an emergent (i.e., $h_g > 2H$) sea grass patch), but by assuming $U(y)$ to be a tanh-profile, and neglecting the viscous term White & Nepf (2007). Previous calculations for terrestrial grass either exclude the vegetation drag in their models Raupach *et al.* (1996), or assume the mean velocity profile *ad hoc* Raupach *et al.* (1996); Py *et al.* (2006). A threshold flow condition is not reported previously either for terrestrial or submerged marine meadows.

(65) The frequency ($\text{Im}(\sigma)$) of the fastest growing mode agrees well with observed frequencies – frequency of *monami*, maxima in the velocity spectra, and frequency of vortex passage in lab scale experiments M. Ghisalberti and H. M. Nepf (2002) – for cases where the vegetation was sufficiently dense to be modeled by a continuum drag field, as shown in the inset in Fig. 2. The experimentally observed *monami* wavelengths are not available for comparison.

	Kelvin-Helmholtz	Mode 1	Mode 2
Base velocity profile	$U(y) = U_0 \tanh(y/\delta)$	Equation (0.2)	
Domain	$-\infty < y < \infty$	$-1 < y < 1$	
Inflection point	exists at $y = 0$	$U''(y)$ discontinuous at $y = h_g$	
Shear layer thickness	δ	$\delta \sim H\left(Re\tilde{N}_g\right)^{-1/3}$	
Linearized dynamics	$(\sigma + ikU)\left(D^2 - k^2\right)\phi = ikU_{yy}\phi$	Equation (0.3)	
Dense grass limit		Equation (0.4)	Equation (0.5)
Critical parameters	none	$Re \propto \tilde{N}_g^2$	$Re \propto \tilde{N}_g$
Most unstable k as $\delta \to 0$	$\propto H/\delta$	$\propto H/\delta$	$O(1)$
Mode localized?	yes, near $y = 0$	yes, near $y = h_g$	no, spans water column

TABLE 1. **(17)** Comparison between Kelvin-Helmholtz instability and the two unstable modes resulting from solution of 0.3.

(140) To better understand the instability mechanism, we consider the dependence of the fastest growing wavenumber on δ. The fastest growing wavenumber first increases proportional to H/δ, but at a critical δ discontinuously jumps and remains $O(1)$ (see Fig. 2). To aid in explaining this behavior, we show heat maps of $\text{Re}(\sigma)$ as a function of Re and k, for different h_g/H and $\tilde{N}_g$ in Fig. 3. The smallest Re on the neutral curve ($\text{Re}(\sigma) = 0$) sets the threshold. We observe that as $\tilde{N}_g$ increases, the unstable region splits into two; we refer to the region with the higher k as "Mode 1", and the one with the lower k as "Mode 2". The unstable region for Mode 1, depending on h_g/H either recedes to higher Re or shrinks to zero size, as the vegetation density increases, causing the most unstable mode to transition discontinuously.

(117) The distinct asymptotic behavior of the two modes as $\tilde{N}_g \gg 1$ distinguishes it from the Kelvin-Helmholtz instability. Mode 1 asymptotically localizes to the boundary layer near the grass top, and exhibits an asymptotic behavior with $k \sim H/\delta$, and $Re(\sim H/\delta)^2$ (or $Re \propto \tilde{N}_g^2$) at the threshold. This limit can be understood by asymptotically estimating the sizes of the terms in (0.3) using $D \sim H/\delta$, $\sigma \sim O(1)$, and $U_{\text{bl}} \sim \delta/H$; the magnitude of the advection term is $Re(H/\delta)^2$ (or $Re^{5/3}\tilde{N}_g^{2/3}$), and the viscous and the vegetation drag term in the boundary layer are $(\delta/H)^{-4}$ (or $(Re\tilde{N}_g)^{4/3}$). The terms balance when $Re \sim (H/\delta)^2$ (or $Re \sim \tilde{N}_g^2$). Using the boundary layer co-ordinate $\eta = y/\delta$, velocity scaling $U(y) = (\delta/H)\bar{U}(\eta)$ and scaling of wavenumber $k = (H/\delta)\bar{k}$ in the boundary layer (0.3) simplifies to

$$\left(\bar{D}^2 - \bar{k}^2\right)^2 \phi = (Re/\tilde{N}_g^2)^{1/3}\left[\left(\sigma + i\bar{k}\bar{U}\right)\left(\bar{D}^2 - \bar{k}^2\right) - i\bar{k}\bar{U}_{\eta\eta}\right]\phi \\ + \bar{D}\left(2S\bar{U}D\phi\right), \tag{0.4}$$

(93) in a region of thickness $O(\delta)$ near $y = h_g$. Since $(Re/\tilde{N}_g^2)$ is the only remaining parameter in (0.4), the mode shape and soultion will converge in the limit of $R \sim \tilde{N}_g^2$, confirming our numerial finding. This analysis also concludes that the mode structure is self-similar over the length scale δ for fixed $Re/\tilde{N}_g^2$; the verification of this idea is shown in Fig. 4 (inset).

(45) Similarly, the threshold condition for Mode 2 is numerically observed to be $Re \propto (\delta/H)^{-3/2}$ (or $Re \propto \tilde{N}_g$) for $k \sim O(1)$, shown in Fig. 2, which can be understood by assuming $Re \gg 1$ but fixed $Re/\tilde{N}_g \sim O(1)$. In this limit (0.3) simplifies to

$$\sigma\left(D^2 - k^2\right)\phi = -2(\tilde{N}_g/Re)^{1/2}D^2\phi, \quad \text{for } y < h_g \\ (\sigma + ikU)\left(D^2 - k^2\right)\phi = ikU_{yy}\phi, \quad \text{for } y > h_g. \tag{0.5}$$
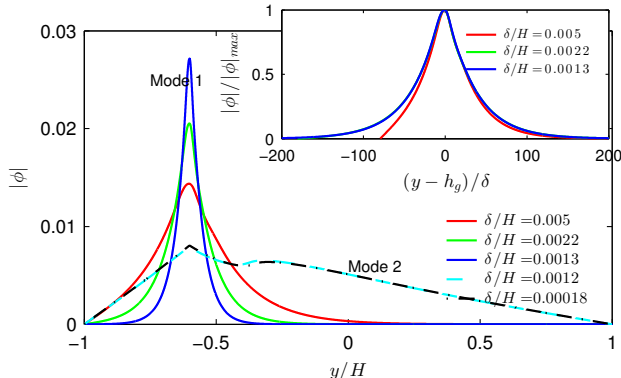
FIGURE 4. **(75)** Plot of the neutral Mode 1 (solid) and Mode 2 (dashed) shape $|\phi|$ in the limit of small δ/H for $h_g/H = 0.2$. The approach of mode shapes to each other for these small values of δ/H indicates that the dense vegetation asymptote is reached. Mode 1 shapes appear self-similar in shape as $\delta \to 0$. Inset shows rescaled $|\phi|$ for Mode 1 as a function of $(y - h_g)/\delta$ approach a universal shape, indicating that an asymptotic limit has been reached.

(54) Similarly here $Re/\tilde{N}_g$ is the only remaining parameter in (0.5), the mode shape converges in the aforementioned limit, in agreement with our numerical results shown in Fig. 4. The parameter $Re/\tilde{N}_g$ also sets the threshold, leading to the asymptotic behavior $Re \propto \tilde{N}_g$ (or $Re \sim (\delta/H)^{-3/2}$; see Fig. 2 for comparison with numerical results).

(122) Table 1 compares the two modes to each other, and to the Kelvin-Helmholtz instability. Because the eigenfunction of Mode 1 is localized over a length scale δ, it may be interpreted as the instability of the flow in the boundary layer, whereas Mode 2 may be understood as the instability on the scale of the water column. Mode 1 appears to be superficially similar to the Kelvin Helmholtz mechanism, whereas Mode 2 arises purely from the interaction between the unvegetated water column and the flow through the vegetation. The appearance of the vegetation drag parameter in the dominant balances represented by (0.4) and (0.5), and the resulting threshold criteria demonstrates its role in setting the threshold, and in distinguishing them from the Kelvin-Helmholtz instability.

(92) The analogous oscillation of terrestrial canopies in wind, known as *honami* Inoue (1956); Raupach *et al.* (1996), is different because the atmospheric boundary layer is much larger than the vegetation height. In the framework of our model, the limit of $h_g/H \ll 1$ while $\delta/h_g = $ constant can be used to represent the hydrodynamic instability for the terrestrial case. We find that in this case, the transition from Mode 1 to Mode 2 happens at such a large vegetation density, so as to make Mode 2 irrelevant. In this manner, we recover the Kelvin-Helmholtz-like characteristics observed in the terrestrial case.

(117) We now test the assumption of an undeformable grass bed due to the dominant restoring force of buoyancy, using the criteria that the buoyancy time scale be much shorter than the hydrodynamic time scale H/U_0. For a common seagrass, *Zostera Marina*, the relative density difference $\Delta\rho/\rho \approx 0.25$, the volume fraction $V_f \approx 0.1$ and $H = 1$ m Fonseca (1998), yielding the buoyancy time scale $\sqrt{\rho H/V_f \Delta\rho g} \approx 2$ s. The hydrodynamic time scale assuming $U_0 \approx 0.1$ m/s is 10 s, and therefore longer than the hydrodynamic time scale. We have neither accounted Accounting for the pre-factors appearing in the scaling argument, or considering cases when the time-scale separation is not so evident can lead to further interesting behavior Py *et al.* (2006).

(104) In conclusion, we show that the hydrodynamic instability underlying *monami* differs from the traditional Kelvin-Helmholtz due to the presence of the vegetation

drag. The threshold flow condition observed in the field and in lab experiments arises due to the presence of this drag. While further investigation is needed to understand the sensitivity of the results to the various simplifying assumptions made in our model, the agreement with experiments is encouraging. Our analysis also informs flow structure formation in many other related scenarios, such as flow over coral reefs, permeable sediments, flow through urban environments and therefore is expected to have a wider impact.

REFERENCES

ACKERMAN, J. D. & OKUBO, A. 1993 Reduced mixing in a marine macrophyte canopy. *Functional Ecology* **7**, 305–309.

DRAZIN, P. G. & REID, W. H. 1981 Hydrodynamic stability. *Cambridge U. Press, Cambridge* .

FONSECA, M. 1998 Exploring the basic pattern expression in seagrass landscape. PhD thesis, University of California, Berkeley.

FONSECA, M. S. & KENWORTHY, W. J. 1987 Effects of current on photosynthesis and distribution of seagrasses. *Aquatic Botany* **27** (1), 59–78, environmental Impacts On Seagrasses.

GHISALBERTI, M. & NEPF, H. M. 2004 The limited growth of vegetated shear layers. *Water Resources Research* **40** (7).

GHISALBERTI, M. & NEPF, H. M. 2006 The sructures of shear layer in flows over rigid and flexible canopies. *Enviornmental Fluid Mechanics* pp. 277–301.

GRIZZLE, R. E., SHORT, F. T., NEWELL, C. R., HOVEN, H. & KINDBLOM, L. 1996 Hydrodynamically induced synchronous waving of seagrasses: 'monami' and its possible effects on larval mussel settlement. *Journal of Experimental Marine Biology and Ecology* **206** (1–2), 165–177.

IKEDA, S. & KANAZAWA, M. 1996 Three-dimensional organized vortices above flexible water plants. *Journal of Hydraulic Engineering* **122** (11), 634–640.

INOUE, E. 1956 Studies of the Phenomena of Waving Plants Caused by Wind. *J. of Agri. Meteor.* **11** (4), 147–151.

M. GHISALBERTI AND H. M. NEPF 2002 Mixing layer and cohrent structures in vegetated aquatic flows. *J. Geophys. Res.* **107**.

NEPF, H. M. 1999 Drag, turbulence, and diffusion in flow through emergent vegetation. *Water resources research* **35** (2), 479–489.

NEPF, H. M. 2012 Flow and transport in regions with aquatic vegetation. *Annual Review of Fluid Mechanics* **44**, 123–142.

NEPF, H. M. & VIVONI, E. R. 2000 Flow structure in depth-limited vegetated flow. *J. Geophys. Res.* **105**, 28,547–28,557.

OKAMOTO, T., NEZU, I. & IKEDA, H. 2012 Vertical mass and momentum transport in open-channel flows with submerged vegetations. *Journal of Hydro-environment Research* **6** (4), 287–297.

PY, C., DE LANGRE, E. & MOULIA, B. 2006 A frequency lock-in mechanism in the interaction between wind and crop canopies. *J. Fluid Mech.* **568**, 425–449.

RAUPACH, M. R., FINNIGAN, J. J. & Y.BRUNET 1996 Cohrent eddies and turbulence in vegetation canopies: The mixing layer analogy. *Boundary-Layer Meteorology* **78**, 351–382.

VIVONI, E. R. 1998 Turbulence structure of a model seagrass meadow. Master's thesis, MIT.

WHITE, B. L. & NEPF, H. M. 2007 Shear instability and coherent structures in shallow flow adjacent to a porous layer. *Journal of Fluid Mechanics* **593**, 1–32.